NEUROSCIENCE

Serotonin rebalances cortical tuning and behavior linked to autism symptoms in 15q11-13 CNV mice

Nobuhiro Nakai,[1,2,3]* Masatoshi Nagano,[4]* Fumihito Saitow,[4]* Yasuhito Watanabe,[2,5]† Yoshinobu Kawamura,[2] Akiko Kawamoto,[2] Kota Tamada,[1,2] Hiroshi Mizuma,[6] Hirotaka Onoe,[6] Yasuyoshi Watanabe,[6] Hiromu Monai,[1] Hajime Hirase,[1] Jin Nakatani,[7] Hirofumi Inagaki,[4] Tomoyuki Kawada,[4] Taisuke Miyazaki,[8] Masahiko Watanabe,[8] Yuka Sato,[9] Shigeo Okabe,[9] Kazuo Kitamura,[9] Masanobu Kano,[9] Kouichi Hashimoto,[2] Hidenori Suzuki,[4,10†] Toru Takumi[1,2,10†]

Serotonin is a critical modulator of cortical function, and its metabolism is defective in autism spectrum disorder (ASD) brain. How serotonin metabolism regulates cortical physiology and contributes to the pathological and behavioral symptoms of ASD remains unknown. We show that normal serotonin levels are essential for the maintenance of neocortical excitation/inhibition balance, correct sensory stimulus tuning, and social behavior. Conversely, low serotonin levels in *15q dup* mice (a model for ASD with the human 15q11-13 duplication) result in impairment of the same phenotypes. Restoration of normal serotonin levels in *15q dup* mice revealed the reversibility of a subset of ASD-related symptoms in the adult. These findings suggest that serotonin may have therapeutic potential for discrete ASD symptoms.

INTRODUCTION

Copy number variation (CNV) is one of the most prevalent genomic abnormalities in autism spectrum disorder (ASD) (*1*–*3*). We previously generated a 15q11-13 duplication model mouse corresponding to one of the most cytogenetically frequent CNVs in ASD (*4*, *5*) and showed that paternal duplication (*15q dup*) mice displayed ASD-like behaviors including poor social communication and interaction, behavioral inflexibility (*6*, *7*), and abnormalities of cortical spines and cerebellar functions (*8*, *9*). We also found a reduction in the level of serotonin [5-hydroxytryptamine (5-HT)] and in the volume of the dorsal raphe nucleus (DRN), which contains a large proportion of 5-HT neurons providing serotonergic projections to cortical forebrain regions (*7*, *10*). A decreased rate of 5-HT synthesis in developmental stages has been reported in the central nervous system of ASD patients (*11*), suggesting a hyposerotonergic state. The 5-HT system also has abnormal modulatory effects on cognitive function in ASD (*12*), and behavioral abnormalities are thought to result from 5-HT–impaired neural networks, although direct evidence is lacking (*13*). Excitation/inhibition (E/I) balance is suggested to be disrupted in ASD (*3*, *14*), and enhancement of the γ-aminobutyric acid (GABA)–ergic system rescues physiological and behavioral deficits in ASD model mice (*15*–*17*). However, the hyposerotonergic state and its physiological and behavioral consequences (particularly for cortical E/I balance and social behavior) remain unexamined in ASD model mice.

[1]RIKEN Brain Science Institute, Wako, Saitama 351-0198, Japan. [2]Graduate School of Biomedical Sciences, Hiroshima University, Minami, Hiroshima 734-8553, Japan. [3]Graduate School of Biostudies, Kyoto University, Sakyo, Kyoto 606-8501, Japan. [4]Graduate School of Medicine, Nippon Medical School, Bunkyo, Tokyo 113-8602, Japan. [5]Department of Clinical Neurobiology, University Hospital and German Cancer Research Center, Heidelberg 69120, Germany. [6]RIKEN Center for Life Science Technologies, Chuo, Kobe 650-0047, Japan. [7]Shiga University of Medical Science, Otsu, Shiga 520-2192, Japan. [8]Department of Anatomy and Embryology, Hokkaido University Graduate School of Medicine, Kita, Sapporo 060-8638, Japan. [9]Graduate School of Medicine, University of Tokyo, Bunkyo, Tokyo 113-8654, Japan. [10]Core Research for Evolutional Science and Technology (CREST), Japan Science and Technology Agency, Tokyo, Japan.
*These authors contributed equally to this work.
†Corresponding author. Email: toru.takumi@riken.jp (T.T.); hsuzuki@nms.ac.jp (H.S.); y.watanabe@dkfz-heidelberg.de (Yasuhito Watanabe)

RESULTS AND DISCUSSION

15q dup mice have reduced excitatory transmission and glucose metabolism in the DRN

We initially measured the electrophysiological properties of 5-HT neurons in the DRN of wild-type (WT) and *15q dup* mice. 5-HT neurons were identified by their firing patterns and action potential shapes, along with subsequent immunohistochemistry with a tryptophan hydroxylase (Tph) antibody (Fig. 1A). The resting membrane potential of *15q dup* neurons was hyperpolarized compared with that of WT neurons (Fig. 1B), whereas other properties related to action potential generation did not differ (table S1) and dendritic complexity of 5-HT neurons was unchanged (fig. S1). We also recorded spontaneous excitatory postsynaptic currents (sEPSCs) from DRN neurons. The sEPSC amplitudes in *15q dup* neurons were smaller in both ventromedial DRN (vmDRN) and lateral wing DRN (lwDRN), whereas sEPSC frequencies showed no changes (Fig. 1, C to E). We assessed DRN activity in vivo by positron emission tomography (PET) imaging of regional cerebral glucose metabolism (rCGM) with a 2-[^{18}F]fluoro-2-deoxy-D-glucose ([^{18}F]FDG) probe. The global brain activity of *15q dup* mice did not significantly differ from that of WT mice (Fig. 1, F and G), but a voxel-based statistical parametric mapping analysis revealed lower rCGM in the DRN of *15q dup* mice (Fig. 1, H, J, L, and M). We also observed increased rCGMs in the hippocampus and anterior cingulate cortex (Fig. 1, H to M), which may reflect elevated levels of anxiety in *15q dup* mice. Together, these results suggest that the hyposerotonergic state in *15q dup* mice is caused by overt low activity of the DRN and may be explained in part by 5-HT neurons receiving a weaker drive from afferent excitatory inputs.

Sensory tuning is impaired in *15q dup* somatosensory cortex barrel field

The reduced DRN activity led us to investigate its impact on downstream cortical areas. We recorded from the somatosensory cortex where the circuit organization is well known to be affected by 5-HT level (*18*), and patients with ASD show poor response reliability in sensory cortical areas (*19*, *20*). Using a transgenic mouse expressing GCaMP7, we measured the reliability of sensory-evoked response tuning in the somatosensory cortex barrel field (S1BF) in *15q dup* mice

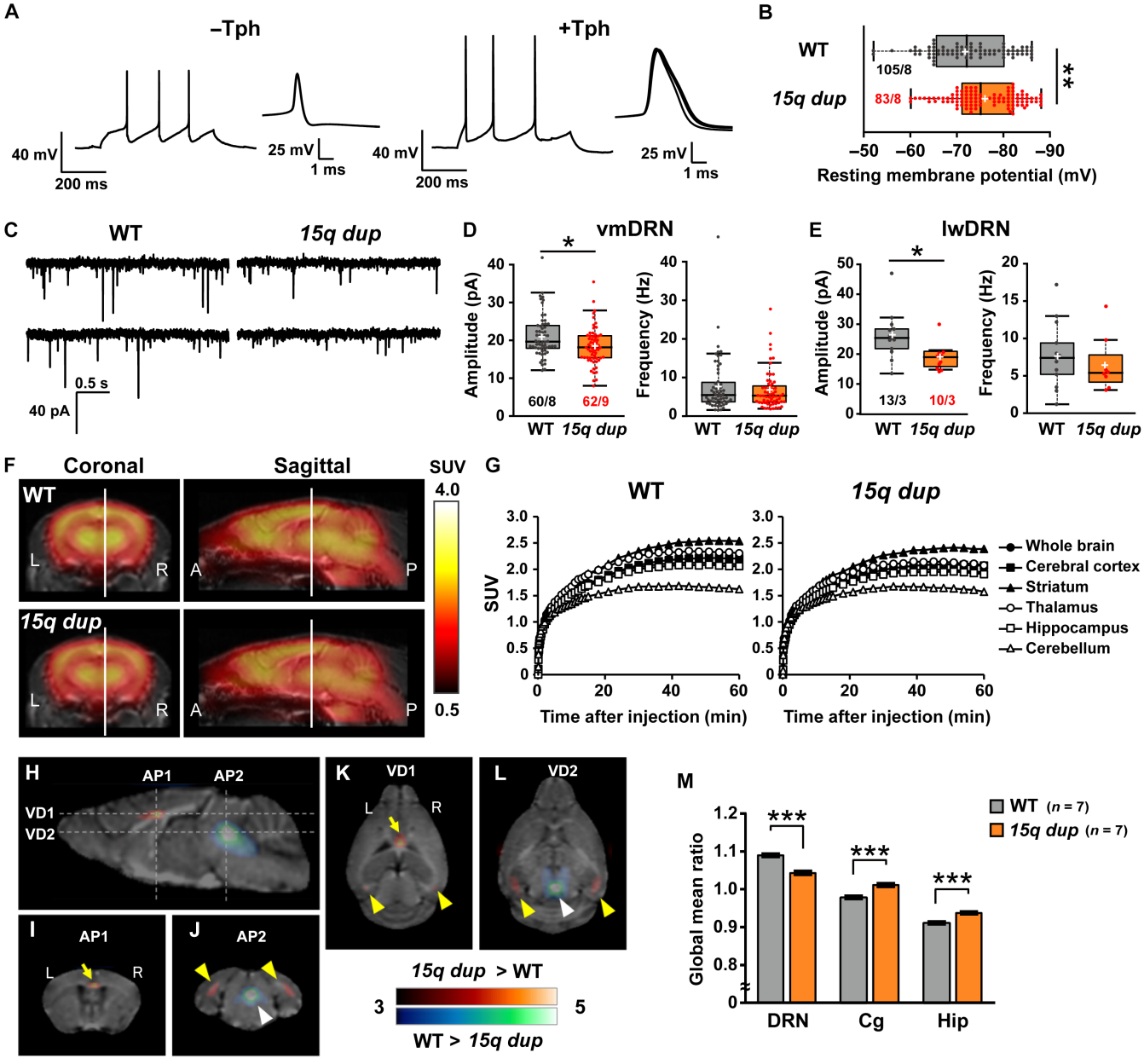

Fig. 1. *15q dup* mice have reduced excitatory synaptic transmission onto 5-HT neurons and low glucose metabolism in the DRN. (**A**) Representative action potential recordings of non–5-HT (Tph-immunoreactive–negative, –Tph) and 5-HT (Tph-immunoreactive–positive, +Tph) neurons in DRN in response to depolarizing current injections of 100 and 140 pA, respectively (left). Individual spikes are aligned at the starting point of spike and displayed in an expanded time scale (right). (**B**) The resting membrane potentials of 5-HT neurons in the DRN were hyperpolarized in *15q dup* mice. $^{**}P < 0.01$, Wilcoxon rank sum test. (**C**) Representative sEPSC traces recorded from 5-HT neurons in DRN. (**D** and **E**) Comparisons between WT and *15q dup* mice for the sEPSC amplitude and frequency in 5-HT neurons obtained from the vmDRN and lwDRN subregions. The amplitude but not the frequency of sEPSCs was decreased in *15q dup* mice at vmDRN ($^{*}P < 0.05$, Brunner-Munzel test) and lwDRN ($^{*}P < 0.05$, Wilcoxon rank sum test). *n* = cells per mice. (**F**) Summed PET images from 30 to 60 min after the [^{18}F]FDG injection were made by averaging the images in each group (*n* = 7 mice, triplicate in each genotype). The heat map indicates the standardized uptake value (SUV) of glucose. (**G**) The graphs show the mean time–radioactivity curves of [^{18}F]FDG. Regions of interest were manually drawn on the [^{18}F]FDG-PET images based on a morphologically normalized coronal magnetic resonance T1-weighted image. (**H**) Maps of the *t* scores obtained by voxel-based statistical comparisons of the [^{18}F]FDG uptake between WT and *15q dup* mice. An unpaired two-sample *t* test was performed. Pseudocolor maps of the *t* scores are fused on a mouse brain magnetic resonance T1-weighted image. (**I** to **L**) The coronal sections correspond to AP1 and AP2 dashed lines in (H) [(I) and (J)], and the horizontal sections correspond to VD1 and VD2 dashed lines in (H) [(K) and (L)]. Low glucose metabolism in the DRN (white arrowheads) of *15q dup* mice was observed compared with that in WT littermates. The *15q dup* mice also showed high glucose metabolism in the anterior cingulate cortex (Cg; yellow arrows) and hippocampal region (Hip; yellow arrowheads). Statistical significance was defined at a threshold of $P < 0.005$ (uncorrected), $t > 3.05$, $F = 12$. (**M**) Differences in [^{18}F]FDG uptake ratios (calculated as regional uptake per whole brain uptake of [^{18}F]FDG) between the two groups (*n* = 7 mice in each group; $^{***}P < 0.001$, two-tailed Student's *t* test). Box plots represent the median and the 25th and 75th percentiles. Each dot represents individual sample data. The mean is represented by a plus sign. Whiskers represent the minimum and maximum values except for outliers. All other values are means ± SEM.

by transcranial calcium imaging (Fig. 2A). The size of the peak response area of the principal barrel to single whisker stimulation (principal area) was unchanged, whereas that of the responded area (surrounding area) was significantly larger in *15q dup* mice (Fig. 2, B and C). Moreover, the peak amplitude was smaller, and the percentage of its decay slope was slower in the principal area in *15q dup* mice (Fig. 2, D to F), indicating that *15q dup* mice have degraded responsiveness to the principal whisker. To evaluate the responsiveness of a single neuron to whisker stimuli, we performed in vivo patch-clamp recordings of layer 2/3 (L2/3) regular spiking neurons of the S1BF (Fig. 2, G and H). In *15q dup* regular spiking neurons, firing properties were normal (table S2), but the amplitudes of surrounding whisker responses (S1Ws) were larger than those in WT mice, whereas the amplitudes of principal whisker responses (PWs) were comparable

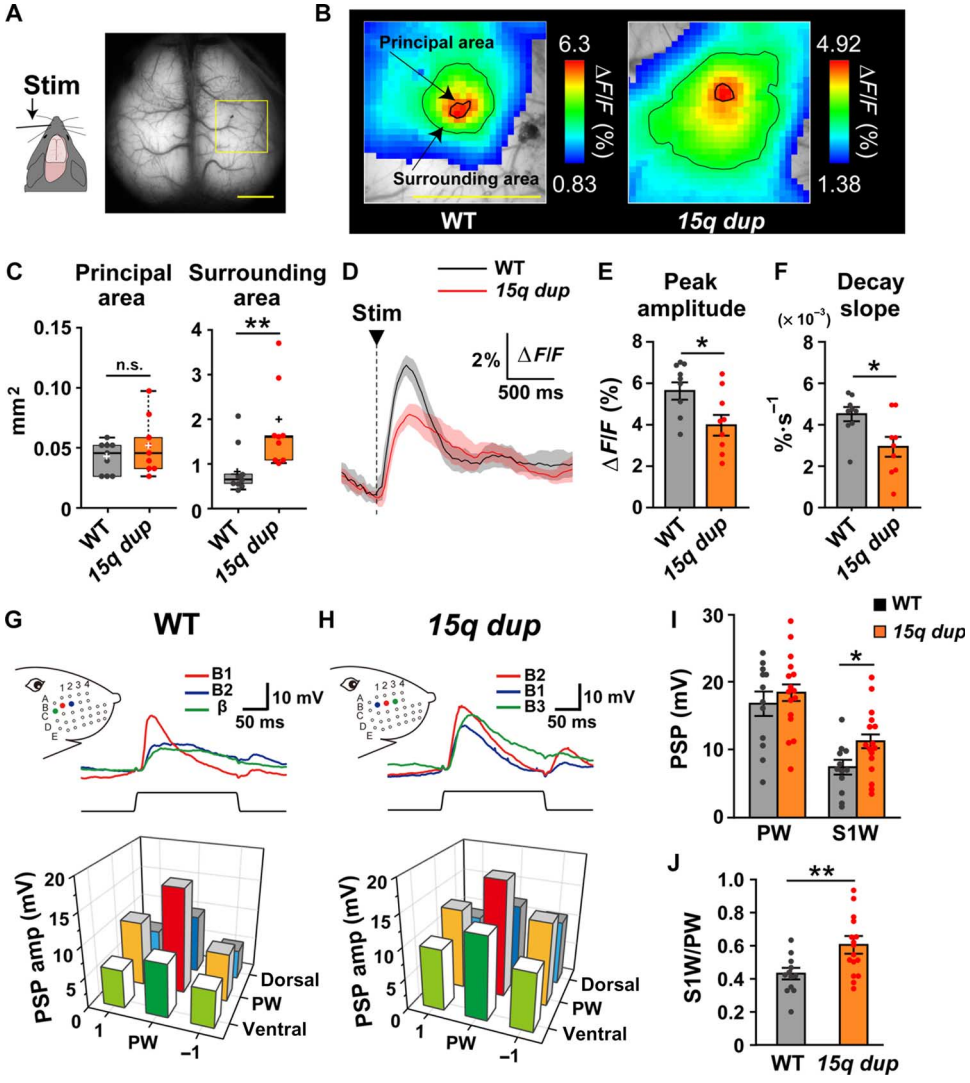

Fig. 2. Sensory-evoked somatosensory receptive field tuning responses are impaired in *15q dup* mice. (**A**) The right barrel field (yellow open square) was analyzed in the transcranial calcium imaging. The left C2 whisker is stimulated by a piezo driver at 10 Hz of 10 pulses and at 0.25 Hz of 20 pulses. Scale bar, 2 mm. (**B**) Representative images of barrel area responses at 10-Hz stimulation in each genotype. The color represents the Δ*F*/*F* of averaged image. The area within the bold line indicates the response in principal barrel, and the area within the fine line indicates the response in surrounding barrels of the C2 whisker barrel. Scale bar, 2 mm. (**C**) The area size of the principal barrel was comparable between genotypes, whereas the area size of the surrounding barrel was larger in *15q dup* mice. $^{**}P < 0.01$, Wilcoxon rank sum test. n.s., not significant. (**D**) The traces indicate the averaged Δ*F*/*F* of the principal barrel (black, WT; red, *15q dup*) at 0.25-Hz stimulation. The faint color indicates SEMs in each genotype. (**E**) The peak amplitude of the principal barrel was smaller in *15q dup* mice. (**F**) The decay slope of the principal barrel was smaller in *15q dup* mice. $^{*}P < 0.05$, two-tailed Student's *t* test. $n = 9$ mice in both genotypes. (**G** and **H**) Top: Superimposed traces show the averaged responses to single whisker deflections of the PW, which has the strongest amplitude and fastest onset latency to the whisker stimuli (red, B1), and the S1Ws, which have weaker amplitudes and slower onset latencies (blue, B2; green, β), in a representative case of WT mice and those to the PW (red, B2) and the S1Ws (blue, B1; green, B3) in a representative case of *15q dup* mice. Insets: Schema indicates the whisker pattern and deflection points. Bottom: Three-dimensional bar graphs show receptive field maps of averaged postsynaptic potential (PSP) amplitudes, centered to the PW. The PSPs of S1Ws in *15q dup* mice showed higher responses than those in WT mice. (**I**) The PSP amplitude of the PW was normal, but that of S1W was increased in *15q dup* mice. (**J**) The ratio of S1W- to PW-PSP amplitudes was increased in *15q dup* mice. WT, $n = 12$ mice; *15q dup*, $n = 16$ mice. $^{*}P < 0.05$; $^{**}P < 0.01$, two-tailed Student's *t* test. Box plots represent the median and the 25th and 75th percentiles. Each dot represents individual sample data. The mean is represented by a plus sign. Whiskers represent the minimum and maximum values except for outliers. All other values are means ± SEM.

(Fig. 2I). In line with the calcium imaging data, the tuning of whisker selectivity was less evident in *15q dup* S1BF (Fig. 2J).

15q dup S1BF has fewer inhibitory synapses and L2/3 pyramidal neurons exhibit intrinsic hyperexcitability

Local inhibition is required for specific responses to whisker stimulation (*21*, *22*). Therefore, we examined whether inhibition is impaired in *15q dup* S1BF. The densities of several types of interneurons in the S1BF were comparable between genotypes (fig. S2). We next analyzed inhibitory synapses by immunostaining for vesicular GABA transporter (VGAT) (Fig. 3A). VGAT puncta density was reduced specifically in L2/3 (Fig. 3, B and E) but not in L4 or L6 of *15q dup* S1BF (Fig. 3, C and D). On the other hand, the density of L2/3 excitatory synapses stained by vesicular glutamate transporter 1 (VGluT1) was unchanged (Fig. 3F). Electron microscopy also supported a reduction of inhibitory synapses in *15q dup* S1BF (fig. S3). To confirm these abnormalities

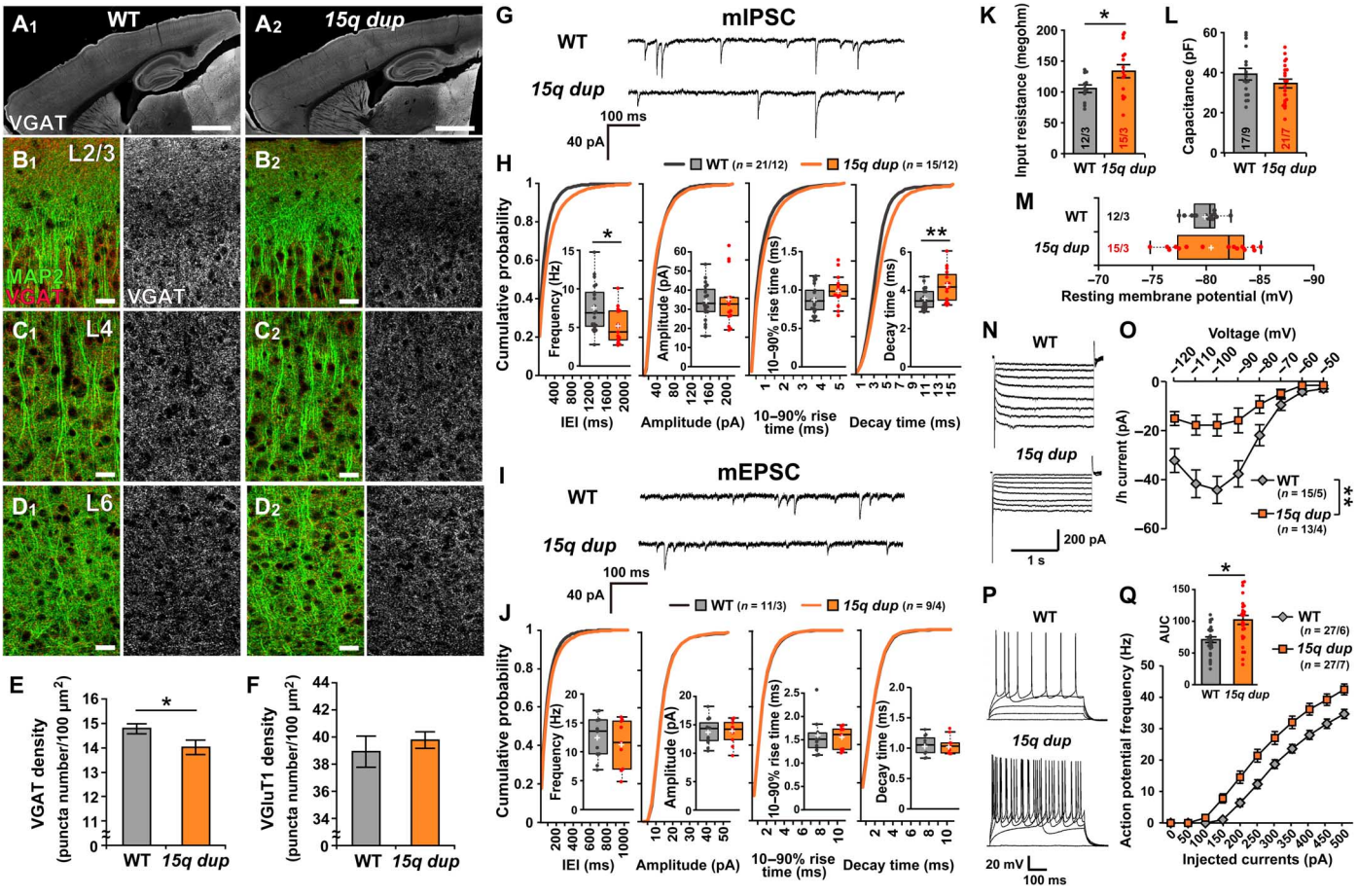

Fig. 3. *15q dup* mice have fewer inhibitory synapses and a higher excitability of pyramidal neurons in L2/3 of somatosensory cortex. (**A** to **D**) Representative images show the S1BF with anti–microtubule-associated protein 2 (MAP2) and anti-VGAT immunostaining [A_1 to D_1 (left column), WT; A_2 to D_2 (right column), *15q dup*]. At low magnification, VGAT signals (white) are comparable between WT (A_1) and *15q dup* (A_2) mice. Scale bars, 1 mm. At high magnification, inhibitory terminals (red, VGAT) on neural dendrites (green, MAP2) in L2/3, L4, and L6 of the S1BF show that only in L2/3 were the VGAT signals weaker in *15q dup* mice (B_2) than in WT mice (B_1). The VGAT signals in L4 (C_1 and C_2) and L6 (D_1 and D_2) were comparable. Scale bars, 20 µm. (**E**) The density of VGAT-positive puncta is reduced in L2/3 of *15q dup* mice (*$P < 0.05$, two-tailed Student's *t* test; $n = 15$ images from five mice per genotype). (**F**) The density of VGluT1-positve puncta was not changed in L2/3 of *15q dup* mice. (**G**) Representative traces of mIPSCs from L2/3 pyramidal neurons in the S1BF of WT and *15q dup* mice. (**H**) The graphs show box plots and cumulative probabilities for mIPSC frequency and basic synaptic responses (amplitude, 10 to 90% rise time, and decay time constant). In *15q dup* mice, the mIPSC frequency was decreased (*$P < 0.05$, two-tailed Student's *t* test), and the cumulative probability of the inter-event interval (IEI) was shifted to the right compared to WT mice. The amplitude and rise time were not changed, but the decay time was increased in *15q dup* mice (**$P < 0.01$, two-tailed Welch's *t* test). (**I**) Representative traces of mEPSCs from L2/3 pyramidal neurons in the S1BF of WT and *15q dup* mice. (**J**) The graphs show box plots and cumulative probabilities for mEPSCs frequencies and basic synaptic responses. There was no difference between genotypes. (**K** to **M**) The graphs show the intrinsic properties of L2/3 pyramidal neurons. The input resistance calculated from the voltage trace in response to the hyperpolarizing current of −50 pA was higher in *15q dup* neurons (K), whereas the cellular capacitance (L) and the resting membrane potential (M) were unchanged. *$P < 0.05$, two-tailed Welch's *t* test. (**N**) Representative traces of the I_h current recorded by the hyperpolarizing voltage steps from −50 to −120 mV. The I_h currents were calculated by dividing the instantaneous current measured at the beginning of the negative voltage step by the steady-state current at the end of the step. (**O**) The I_h currents were smaller in *15q dup* neurons [genotype: $F_{1,26} = 9.495$, **$P < 0.01$, two-way repeated-measures analysis of variance (ANOVA)]. (**P**) The representative voltage traces of L2/3 pyramidal neurons of WT and *15q dup* S1BF in response to current injections with amplitudes from 0 to 400 pA with 100-pA steps. (**Q**) The action potential frequencies are plotted against amplitudes of depolarizing currents. Inset: The area under the curve (AUC) in the line graph was larger in *15q dup* mice (*$P < 0.05$, two-tailed Welch's *t* test). *n* = cells per mice. Box plots represent the median and the 25th and 75th percentiles. Each dot represents individual sample data. The mean is represented by a plus sign. Whiskers represent the minimum and maximum values except for outliers. All other values are means ± SEM.

at the functional level, we recorded miniature inhibitory postsynaptic currents (IPSCs) and EPSCs (mIPSCs and mEPSCs, respectively) from L2/3 pyramidal neurons in the S1BF (Fig. 3, G to J). The frequency of mIPSCs was significantly decreased in *15q dup* mice, although the amplitude and 10 to 90% rise time were unchanged (Fig. 3H). The paired-pulse ratio of evoked IPSCs in *15q dup* mice was the same as that of WT (fig. S4), suggesting normal release probabilities of inhibitory synapses. We found that the decay of mIPSCs was slower in *15q dup* mice (Fig. 3H), which may be induced by the differential expression of GABA type A ($GABA_A$) receptor subunits located in the duplicated chromosome because of the longer decay time constant of the α5 subunit (fig. S5) (*23*). Consistent with histology, the electrophysiological properties of mEPSCs were comparable between genotypes (Fig. 3J). The *15q dup* neurons showed higher input resistance (Fig. 3K), whereas the cellular capacitance and the resting membrane potential were comparable with WT neurons (Fig. 3, L and M). The *15q dup* neurons also had smaller hyperpolarization-activated cation (I_h) currents (Fig. 3, N and O) and decreased dendritic length (fig. S6), similar to those in autism-associated SHANK3 knockout mice (*24*). Consistent with these findings, the intrinsic excitability of L2/3 pyramidal neurons was higher in *15q dup* mice (Fig. 3, P and Q). Collectively, these morphological and electrophysiological abnormalities may contribute to the underlying mechanisms of reduced response tuning specificity to whisker stimuli.

Serotonin modulation ameliorates local synaptic transmission in *15q dup* mice

How are the electrophysiological abnormalities related to the hyposerotonergic state of the *15q dup* mouse? We examined whether *15q dup* mice have alterations in 5-HT responsiveness. Gene expression of 5-HT receptors in *15q dup* brain was unchanged (fig. S7). In *15q dup* mice, 5-HT application enhanced the frequency of spontaneous IPSCs (sIPSCs) (fig. S8, A to F) and suppressed the intrinsic excitability of S1BF pyramidal neurons (fig. S8, G and H), suggesting that compensatory mechanisms took place in *15q dup* cortex in response to the hyposerotonergic state.

The cortical physiology results indicated the potential of 5-HT intervention for restoring cortical E/I balance and behavior. To examine this possibility, we administered the selective serotonin reuptake inhibitor (SSRI) fluoxetine (FLX) to infant mice through their mothers via milk to increase extracellular 5-HT levels (Fig. 4A) because the previously observed 5-HT reduction in *15q dup* mice was seen from postnatal 1 to 3 weeks (*7*). The serum levels of FLX and norfluoxetine (a metabolite of FLX) in the treated offspring were 6.4 ± 6.4 and 220 ± 38 ng/ml at 2 weeks old and 43 ± 23 and 320 ± 70 ng/ml at 3 weeks old, respectively, and neither FLX nor norfluoxetine was detected in serum 1 week after the last treatment. These results indicate that FLX was substantially transferred to offspring mice. Notably, the mIPSC frequency of L2/3 pyramidal neurons in the S1BF was ameliorated in *15q dup* mice treated with FLX (FLX–*15q dup*) but not in the *15q dup* mice treated with vehicle (Veh–*15q dup*; Fig. 4, B and C). FLX treatment did not change the amplitude and rise time of mIPSCs. The decay time constant of FLX–*15q dup* was longer than that of FLX-WT but not significantly different from that of Veh-WT (Fig. 4, B and C). These results indicate that the FLX treatment affects inhibitory synaptic connections rather than synaptic strength in *15q dup* S1BF. Next, we examined 5-HT neurons in the DRNs. The resting membrane potential of FLX–*15q dup* was hyperpolarized compared with that of FLX-WT (Fig. 4D). However, the sEPSC amplitudes at both vmDRN and lwDRN of FLX–*15q dup* mice were comparable to those of FLX-WT (Fig. 4, E and F). Together, these results indicate that increasing the extracellular 5-HT rescued electrophysiological phenotypes of *15q dup* mice by modifying inhibitory transmission in the S1BF and excitatory transmission in the DRN.

Early serotonergic intervention improves social behaviors in *15q dup* mice

Finally, we investigated whether early 5-HT intervention in *15q dup* adult mice could be effective at the behavioral level. We first confirmed the restored levels of 5-HT and its metabolite, 5-hydroxyindoleacetic acid (5-HIAA), in FLX–*15q dup* mice (Fig. 5A). In the three-chamber social interaction (3-CSI) test, FLX–*15q dup* mice spent more time around the cage with a novel mouse than around the empty cage (Fig. 5B), indicating that sociability of *15q dup* mice was rescued by FLX treatment. In the Morris water maze (MWM), all groups showed a normal performance in the learning phase (Fig. 5, C and D), whereas both FLX-WT and FLX–*15q dup* mice exhibited no difference in the length of stay between the target and opposite quadrants in the reversal learning phase, as did the Veh–*15q dup* mice (Fig. 5E). In the open-field test, the FLX treatment induced lower exploratory activity in both WT and *15q-dup* mice (Fig. 5F, left). The time spent in the center of the open field was decreased only in FLX–*15q dup* mice (Fig. 5F, middle). The "anxiety index," which is calculated by normalization of the distance traveled in the center of the open field by the total distance traveled, was significantly decreased in FLX–*15q dup* mice (Fig. 5F, right), indicating that they show an increase in anxiety. These results suggest that FLX has not only positive but also negative effects on certain behaviors such as behavioral flexibility and exploratory behavior. We also examined the effect of FLX treatment on communication behavior in pups by daily injection using two dosages (0.5 and 2.5 mg/kg). Veh–*15q dup* mice exhibited a larger number of ultrasonic vocalizations (USVs) (Fig. 5G), which may reflect higher anxiety levels or fear in response to stress, as previously reported (*6*). The FLX treatment during the first 6 days after birth decreased the number of *15q dup* USVs at postnatal day 7 (P7) in a dose-dependent manner (Fig. 5G), suggesting that FLX treatment can ameliorate anxiety-like behaviors in infant *15q dup* mice.

Serotonergic neuromodulation of the cortical E/I balance in *15q dup* mice

In summary, we identified an essential role for 5-HT in coordinating a broad and plastic subset of ASD-related physiological and behavioral phenotypes in 15q11-13 duplication mice (Fig. 5H). Our electrophysiological results suggest that the cortical E/I balance of *15q dup* mice is shifted to an excitatory state due to decreased inhibitory connections and intrinsic hyperexcitability of pyramidal neurons, which is affected by a weakened 5-HT system. Effects of the serotonergic system on the cerebral cortex remain unclear because 5-HT receptors have heterogeneity in their function and diversity of their expression (*13*). Regarding the major receptors, it is suggested that the $5\text{-}HT_{1A}$ receptor can suppress the excitability of pyramidal neurons and that $5\text{-}HT_{2A}$ and $5\text{-}HT_{2C}$ receptors can enhance interneuron activity in the rat prefrontal cortex (*25*), which may be associated with acute serotonergic modulation in the S1BF of *15q dup* mice (see fig. S8). Such serotonergic neuromodulation was focused in the study of regulatory mechanisms in sensory systems (*26*). The increased E/I ratio is associated with an abnormal sensory system in ASD (*27*, *28*), and disruption of inhibitory circuits is potentially associated with abnormalities in cortical

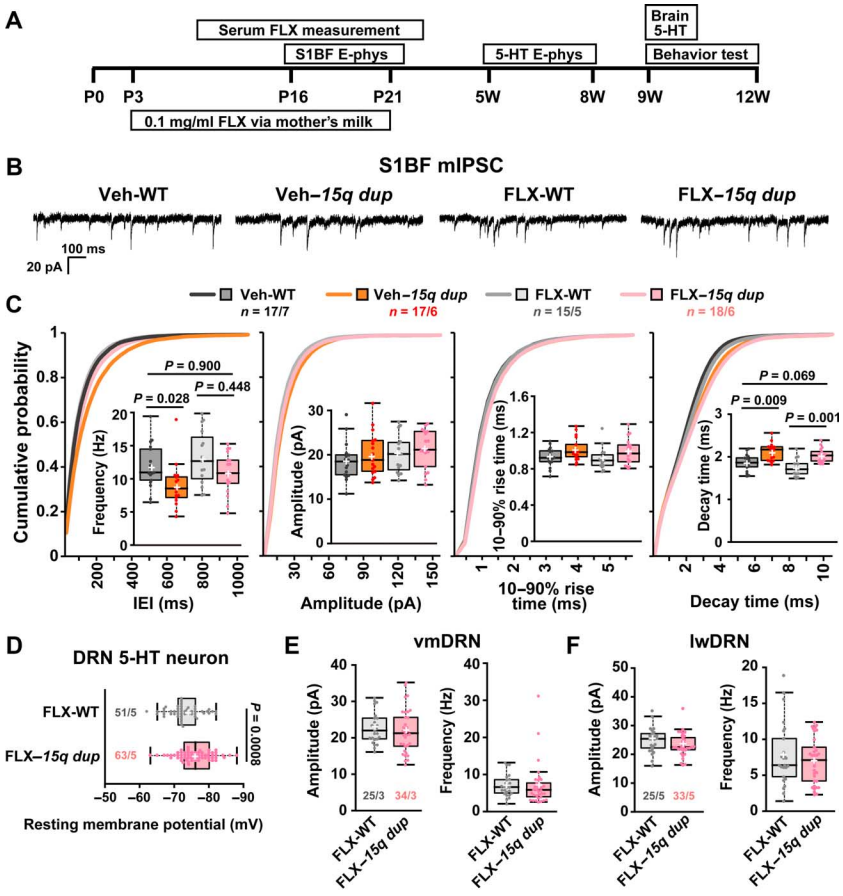

Fig. 4. Chronic FLX treatment during developmental stages restores local synaptic transmission in *15q dup* mice (**A**) The administration of FLX via the mother's milk was started at P3 and finished at P21 (bottom rectangle). The upper rectangles indicate each experimental period. E-phys, electrophysiology. (**B**) The representative traces of mIPSCs from L2/3 pyramidal neurons in the S1BF of vehicle-treated WT (Veh-WT), vehicle-treated *15q dup* (Veh–*15q dup*), FLX-treated WT (FLX-WT), and FLX-treated *15q dup* (FLX–*15q dup*) mice. (**C**) The graphs show box plots and cumulative probabilities for mIPSC frequency and basic synaptic responses from the treated mice. The mIPSC frequency of Veh–*15q dup* was significantly lower, but the mIPSC frequency of FLX–*15q dup* was comparable with that of Veh-WT. The amplitude and rise time of mIPSCs were not changed among these groups. The decay time of FLX–*15q dup* was not significantly different from that of Veh-WT but still longer than that of FLX-WT mice. *P* values were obtained by Steel-Dwass test. (**D**) The hyperpolarized resting membrane potential of DRN 5-HT neurons in *15q dup* mice was not changed by the FLX treatment. *P* value was obtained by two-tailed Student's *t* test. (**E** and **F**) The FLX treatment ameliorated reduction in sEPSC amplitude of *15q dup* mice. The sEPSC amplitudes in 5-HT neurons at vmDRN and lwDRN of FLX–*15q dup* were comparable with FLX-WT mice. There was no difference in sEPSC frequency between groups at both vmDRN and lwDRN. *n* = cells per mice. Box plots represent the median and the 25th and 75th percentiles. Each dot represents individual sample data. The mean is represented by a plus sign. Whiskers represent the minimum and maximum values except for outliers.

processing (*29*). Our findings further strengthen these associations, because *15q dup* mice exhibited inaccurate sensory processing. However, the chronic effect of altered 5-HT levels is not well studied at the in vivo circuit level. Thus, further investigation on whether the recovered inhibitory connections ameliorate sensory response in the FLX-treated mice should be undertaken in future studies.

Our findings also suggest that a subset of ASD-like behaviors, including reduced social behavior and abnormal communication behavior in infant stages but not elevated anxiety in adulthood and behavioral inflexibility, is caused by reduced 5-HT levels. Recovery of the 5-HT system in *15q dup* mice may extend to cortical regions associated with higher brain function [for example, medial prefrontal cortex (mPFC)]. It is reported that 5-HT exerts a potent control on slow and gamma oscillations through 5-HT_{1A} and 5-HT_{2A} receptors in the rat secondary motor cortex and mPFC (*30*). Moreover, optogenetically elevated E/I balance of mPFC induces social dysfunction in WT mice (*31*). There is a possibility that abnormal E/I balance in mPFC of *15q dup* mice, which is induced by low 5-HT as in the case of S1BF, can affect social behavior and that it can be recovered by FLX treatment. This hypothesis will be interesting to examine in future studies.

Potential for developmental therapeutic intervention in the 5-HT system of ASD

Our results reveal the potential of developmental therapeutic interventions in the 5-HT system to restore normal cortical E/I balance and behavior in ASD, although it is difficult to simply apply the strategy used in this study to humans. Clinical studies of SSRIs for ASD have not reached unified conclusions (*32*), and to further develop therapeutic methods for SSRIs, it will be essential to understand their downstream output mechanisms, such as the oxytocin system, on regulating social interaction phenotypes and other relevant behaviors.

Several candidate genes are located within the duplicated chromosome in *15q dup* mice that may be linked to 5-HT abnormalities. Among the paternally expressed genes, *Magel2* and *Ndn* may play a

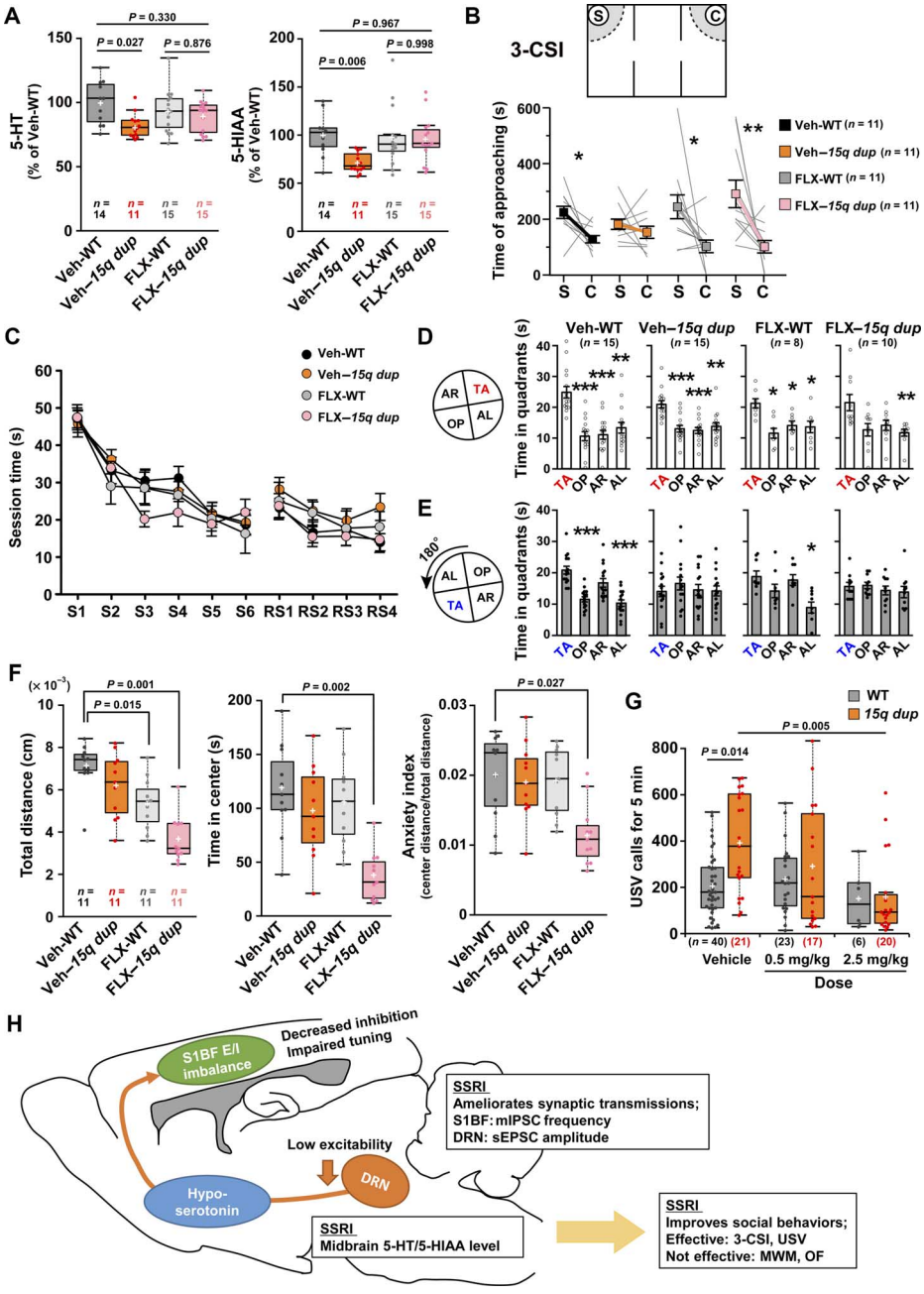

Fig. 5. Restoration of 5-HT level improves social behaviors of *15q dup* mice. (**A**) The tissue levels of 5-HT and 5-HIAA in the midbrain at 9 weeks of age were examined. Veh–*15q dup* showed a reduction in 5-HT levels (left) and 5-HIAA levels (right), whereas FLX–*15q dup* showed no difference in both levels compared with Veh-WT. *P* values were obtained using the Games-Howell test. (**B**) Approaching time to the stranger cage (S) and the empty cage (C) in the 3-CSI test was compared in each group. Only in Veh–*15q dup* was there no difference in approaching time to both cages, whereas others showed increased approaching time to the stranger cage. **P* < 0.05; ***P* < 0.01, exact Wilcoxon signed-rank test. (**C**) The graph shows the performance in training sessions in MWM. S1 to S6, 6 days of learning sessions; RS1 to RS4, 4 days of reversal learning sessions. (**D**) Probe test performance in the MWM test. Configuration of the four quadrants in the probe test after the original training is shown on the left (TA, target quadrant; OP, opposite quadrant; AR, adjacent right quadrant; AL, adjacent left quadrant). The white bar graphs show the times spent in each quadrant. Veh-WT, Veh–*15q dup*, and FLX-WT groups spent more time in the TA compared with the other quadrants, whereas FLX–*15q dup* did not show significance in both OP and AR quadrants. (**E**) Configuration of the four quadrants in the reversal probe test is shown on the left. Only the Veh-WT group showed a significant difference between TA and OP. **P* < 0.05; ***P* < 0.01; ****P* < 0.001, comparison with TA in Steel test. (**F**) Left: The graph shows total distance in open-field test. Exploratory activity in FLX-treated groups was decreased compared with Veh-WT. Middle: The graph shows time spent in the center area in open field (OF). Only FLX–*15q dup* mice showed reduction of the time in center. Right: FLX–*15q dup* mice also showed reduction in the anxiety index, in which the distance traveled in the center area is divided by total distance traveled, for clarification of reduction of the time in center. *P* values compared with Veh-WT were obtained by Steel test. (**G**) The number of USV calls in *15q dup* pups was larger than that in WT mice in the vehicle group, whereas there was no difference in USV calls between genotypes among FLX-treated groups. The USV calls of *15q dup* pups were gradually decreased by FLX dosage (0.5 and 2.5 mg/kg). *P* values were obtained using the Games-Howell test. (**H**) The diagram of this study. *n* = number of mice. Box plots represent the median and the 25th and 75th percentiles. Each dot represents individual sample data. The mean is represented by a plus sign. Whiskers represent the minimum and maximum values except for outliers. All other values are means ± SEM.

role for the pathogenesis of *15q dup* mice because their cognate mutant mice have abnormalities in the 5-HT system (*33*, *34*). A selective duplication, including these genes, was recently reported in two autistic patients (*35*). Future studies will examine the functional roles of genes within the duplicated CNV region in 5-HT–dependent neuron and circuit development, synaptic activity and behavior, and their therapeutic potential in reversing discrete ASD symptoms.

MATERIALS AND METHODS

Animals

All procedures for animal experiments were carried out in accordance with the guidelines of the Animal Experimentation Committee of Nippon Medical School, Hiroshima University, RIKEN Brain Science Institute, and Kobe Institute. The generation of paternal 15q11-13 duplication mice (*15q dup*) was reported previously (*6*), and the line was maintained by mating male *15q dup* with WT female C57BL/6J mice. All mice were maintained on a 12-hour light/dark cycle, and food and water were available ad libitum. For [^{18}F]FDG-PET imaging, 3- to 5-month-old male mice were used. To fix brain volumes of the habituated awake mice for the scanning, these aged mice were needed. For transcranial imaging, 7- to 8-week-old mice were used. For electrophysiology of 5-HT neurons, 5- to 8-week-old mice were used. For in vivo electrophysiology, 4- to 8-week-old mice were used. For immunohistochemistry and electrophysiology of the S1BF, 2- to 3-week-old mice were used. To ensure quality of in vitro and in vivo electrophysiology using patch-clamp recordings, young aged mice were needed. For monoamine measurement and adult behavior tests, 9- to 12-week-old mice were used. Age-matched littermates were used for all experiments.

Chronic drug treatment

FLX hydrochloride (0.1 mg/ml) (LKT Laboratories) in the drinking water including 0.2% saccharin was used except for the USV test. The FLX water was administered to mothers as previously described (*36*). The offspring were treated with FLX through their mothers via milk. Saccharin was used as control drinking water to promote drinking; otherwise, mothers disfavored the FLX water. The saccharin water was not used as drinking water under conventional breeding conditions except for this experiment. FLX treatment was initiated at P3 and terminated at P21. After weaning at P21, the offspring were divided into groups of two to five per cage depending on the treatment and were thereafter fed with normal water. For the USV test, pups were treated with FLX [0.5 or 2.5 mg/kg dose diluted in phosphate-buffered saline (PBS)] by daily intraperitoneal injection from P1 to P6.

PET imaging for glucose metabolism

A head-holder attachment for fixation of the head during PET scanning was placed on the skull of the mouse under 1.5% isoflurane anesthesia using a stereotaxic instrument (SR-6N, Narishige) at least 7 days before the PET experiments as previously described (*37*). Each mouse, which had been well-trained and acclimated to the head-fixation apparatus several times, was fasted for 12 hours and catheterized with a 30-gauge stainless steel needle with a polyethylene tube into the tail vein for injection of [^{18}F]FDG before the PET scan. The mouse was set on the apparatus with head fixation in a small-animal PET scanner (microPET Focus 220, Siemens Medical Systems). A transmission scan for attenuation correction was performed for 30 min using a ^{68}Ge-^{68}Ga point source before the emission scan, and [^{18}F]FDG at a dose of 12 to 15 MBq in 0.1 ml of physiological saline was intravenously injected via the catheter for 10 s using a syringe pump. A dynamic emission PET scan was then performed for 60 min in triplicate for each mouse on separate days. The PET images were reconstructed using a filtered back-projection algorithm with attenuation and no scatter correction for quantitative evaluation of [^{18}F]FDG uptake. Data analysis was performed on seven mice in each group. Two of nine mice in each group were excluded from the data analysis because their blood glucose levels showed higher concentrations (no less than 100 mg/dl) before the beginning of the PET scan. For quantitative analysis of the rCGM, we evaluated the standardized uptake value of glucose as an index and compared the values between *15q dup* and WT mice using PMOD image analysis software (version 3.4; PMOD Technologies Ltd.). Each PET image was co-registered to an FDG-mean image template created using all PET images in the experiment. For identification of the rCGM, a typical mouse brain magnetic resonance T1-weighted image obtained with a 3-T magnetic resonance imaging system (Signa Horizon Lx VH3, GE Healthcare) from an age- and sex-matched mouse of the same strain was used. To identify the precise locations of brain regions showing statistical significance, averaged PET images made by left-right flipping were used. A broader analysis of the rCGM was performed by a two-group comparison test using SPM8 software (Wellcome Trust Centre for Neuroimaging, University College London, London, UK).

Immunohistochemistry

Three-week-old male mice were anesthetized and transcardially perfused with PBS followed by 4% paraformaldehyde (PFA) in 0.1 M phosphate buffer (pH 7.4). Brains were removed and immersion-fixed with 4% PFA at 4°C overnight, cryoprotected with 30% sucrose in PBS for 2 days at 4°C, embedded in an OCT (optimum cutting temperature) compound (Tissue-Tek, Sakura Finetechnical), and frozen in powdered dry ice. Coronal or sagittal sections (30 μm thick) were made using a cryostat and collected in PBS containing 0.01% NaN_3 and stored at 4°C until use. Sections were treated with 0.3% H_2O_2 in PBS for 30 min, washed with PBS for 5 min three times, incubated with a blocking solution (PBS containing 3% normal goat or donkey serum and 0.3% Triton X-100) for 30 min at room temperature, and incubated with primary antibodies diluted with the blocking solution overnight at 4°C. Sections were washed with PBS containing 0.3% Triton X-100 (PBST) for 10 min four times, incubated with fluorescent-conjugated secondary antibodies diluted with the blocking solution for 1 hour at room temperature, washed with PBST for 10 min four times, transferred onto SuperFrost slides, and mounted with VECTASHIELD (Vector Laboratories). The sections were imaged with an FV1000 (Olympus) confocal microscope for puncta analysis and with a BZ8100 fluorescent microscope (Keyence) for cell counting. The images were analyzed using ImageJ software.

Antibodies

Anti-VGluT1 mouse monoclonal antibody (1:1000 dilution; catalog no. 135311, Synaptic Systems), anti-VGAT rabbit polyclonal antibody (1:1000 dilution; catalog no. AB5062P, Millipore), anti-VGAT rabbit polyclonal antibody (1:200 dilution; catalog no. VGAT-Rb-Af500, Frontier Institute), anti-MAP2 goat polyclonal antibody (1:200 dilution; catalog no. MAP2-Go-Af86, Frontier Institute), anti-Tph sheep polyclonal antibody (1:1000 dilution, Life Technologies), anti-GAD67 mouse monoclonal antibody (1:500 dilution; catalog no. MAB5406, Millipore), anti-parvalbumin mouse monoclonal antibody (1:1000 dilution; catalog no. MAB1572, Millipore), anti-somatostatin rabbit polyclonal

antibody (1:100 dilution; catalog no. AB5494, Millipore), and anti–vasoactive intestinal peptide rabbit polyclonal antibody (1:200 dilution; catalog no. 20077, ImmunoStar) were used for primary antibodies. Alexa Fluor 488–conjugated goat anti-mouse immunoglobulin G (IgG) (1:500 dilution; catalog no. A-11017, Invitrogen), Alexa Fluor 488–conjugated donkey anti-sheep secondary antibody (1:1000 dilution, Life Technologies), Alexa Fluor 568–conjugated goat anti-rabbit IgG (1:500 dilution; catalog no. A-21069, Invitrogen), Alexa Fluor 488–conjugated donkey anti-goat IgG (1:500 dilution; catalog no. A-11055, Invitrogen), and Cy3 AffiniPure donkey anti-rabbit IgG (1:500 dilution; catalog no. 711-165-152, Jackson ImmunoResearch) were used for secondary antibodies.

Puncta analysis

L2/3 of S1BF (bregma, −1.34 to −1.82 mm; lateral direction, 2.5 to 3.5 mm) of male mice at P21 was imaged with an FV1000 (Olympus) confocal laser scanning microscope at 60× magnification digitally zoomed 1.6 times. For VGluT1 puncta analysis, a total of 150 images at 512 × 512 pixels were acquired from five mice per genotype. For VGAT puncta analysis, a total of 15 images were acquired from five mice per genotype. Using the area selection tool of ImageJ software, 108 × 108 pixel areas (688.75 μm^2) devoid of somata were selected and converted into binary data with a certain threshold. The threshold was determined to outline as many immunopositive puncta as possible throughout all images with subsequent linearity check, where the linear increase of the number of puncta as a function of the number of image stacks was tested (focal planes taken at a distance of 1 μm). The experiment and analysis were performed without knowledge of the genotype.

Transcranial calcium imaging

Seven- to eight-week-old G7NG817 heterozygote male and female mice (*38*), which were bred from male *15q dup* mice and female G7NG817 heterozygote mice, were used for calcium imaging. Mice were anesthetized with urethane [1.5 g/kg, intraperitoneally (ip); 15% solution in PBS buffer], fixed to a stereotaxic stage by the ear bar, and placed under a fluorescence stereomicroscope (MZ10F, Leica). The GFP3 filter set (excitation, 470 ± 20 nm; emission, 525 ± 25 nm; Leica) was used with the EL6000 light source (Leica). Images were acquired using the ORCA-Flash 2.0 CMOS camera (Hamamatsu Photonics) using HC Image software (Hamamatsu Photonics). The HC Image software also controlled a shutter unit to illuminate the skull only during imaging. Images were acquired with a size of 512 × 512 pixels and 16-bit resolution at a 30-Hz frame rate. The left C2 whisker was cut at 10 mm above the skin, and the surrounding whiskers were trimmed. By the custom device made out of a piezo driver, the C2 whisker was backwardly deflected 20 times with a 200-ms duration at a frequency of 1 Hz and 10 times with a 25-ms duration at 10 Hz and repeated 16 times at an interval of 30 s.

The original 512 × 512 pixel images were reduced to 64 × 64 pixels by binning. The ratio of the relative fluorescent change and the baseline fluorescence ($\Delta F/F$) was calculated by taking the baseline (F) as the signal 500 ms before the stimulus presentation. For the analysis of sensory-evoked response area, the principal area is defined as the region that exceeds the mean response in the 3 × 3 binned area around the peak value during 500 ms from the stimulus onset; the surrounding area is defined as the region that exceeds 60% of the mean peak amplitude during 500 ms from the stimulus onset. In this analysis, the principal area size in WT mice was about 0.04 to 0.05 mm^2, which is consistent with the histological C2 barrel size. To compute the decay slope, the mean whisker-evoked responses for respective periods were normalized to their peak value. Pseudocoloring was carried out using Origin 9.0 (OriginLab).

In vivo electrophysiology

Male and female littermates (4 to 8 weeks old) were used. Mice were anesthetized with urethane [1.5 g/kg, ip; 15 to 20% solution was prepared in Hepes-buffered saline containing 150 mM NaCl, 2.5 mM KCl, 10 mM Hepes, 2 mM $CaCl_2$, and 1 mM $MgCl_2$ (pH 7.3)]. The depth of anesthesia was monitored by vibrissa movements and withdrawal reflex to hindlimb pinch. Body temperature was maintained at 37° ± 1°C using a heating pad. The animal's head was fixed on a stereotaxic apparatus using ear bars (Narishige). After cutting the skin and removing muscles and connective tissues, the skull over the cerebral cortex was exposed. Lidocaine gel was applied to the skin incision. A craniotomy (diameter, 1 to 2 mm) was performed by using a microdrill (NSK) to expose a barrel cortex at 3.5 to 4 mm lateral and 1 to 1.5 mm posterior from the bregma. Subsequently, the dura was cut using a 30-gauge syringe needle and fine forceps. The craniotomy was then filled with 1.5% low–melting point agarose dissolved in Hepes-buffered saline as described above. Whole-cell patch-clamp recordings were made with a Multiclamp 700B amplifier (Molecular Devices) by in vivo blind patch-clamp techniques as previously described (*39*, *40*). Briefly, a high positive pressure (100 to 200 mbar) was applied to the pipette to prevent tip occlusion while penetrating the agarose and the pia. After passing the pia, the positive pressure was immediately reduced (25 to 35 mbar) to prevent cortical damage. The pipette advanced in 2-μm steps, and monitoring pipette resistance was used for searching target cells under voltage-clamp mode with a square voltage step (10 mV, 20-ms duration at 50 Hz). When current pulse amplitude decreased suddenly (20 to 50%), quick removal of the positive pressure (following gentle suction, if required to obtain tight seals) resulted in a gigohm seal (>1 gigohm). After cell-attached configuration, whole-cell configuration was obtained by the breaking of the patch membrane using a slow ramp of negative pressure. The resistance of the patch pipette was 5 to 10 megohms when filled with one of the internal solutions with the following compositions: 135 mM K-D-gluconate, 4 mM KCl, 10 mM Hepes, 10 mM Na_2-phosphocreatine, 4 mM Mg–adenosine triphosphate (ATP), and 0.3 mM Na_3–guanosine triphosphate (GTP) (pH 7.3). Liquid junction potential (7 mV) was not corrected. Series resistance was typically 20 to 100 megohms. Electrophysiological data were filtered at 10 kHz and digitized at 20 or 50 kHz with an ITC-18 interface (Instrutech) and acquired with AxoGraph X software (AxoGraph Scientific). Data were analyzed with AxoGraph X, Microsoft Excel (Microsoft), and OriginPro (OriginLab). Single whisker deflection was performed by a voltage step with a 10 to 90% rise of 4.5 ms to a piezoelectric stimulator with an attached glass capillary (*41*). The deflection point of the whisker was about 5 mm from its base. The whisker was deflected backward by 0.8 mm for 200 ms at a frequency of 0.5 Hz and repeated typically 10 to 20 times consecutively. The peak amplitude of whisker-evoked PSP was calculated from averaged traces within 100 ms from stimulation onset. The principal whisker was identified as the whisker-evoking, shortest-latency PSP. The analysis was performed blind to genotype.

In vitro electrophysiology on 5-HT neurons

Brain slices for experiments were prepared from 5- to 8-week-old male mice as previously described (*42*). The mice were deeply anesthetized

by halothane inhalation (~2% in air, v/v) for decapitation. The brains were rapidly removed and placed in ice-cold Na^+-deficient saline (~4°C) containing the following compounds: 252 mM sucrose, 21 mM $NaHCO_3$, 3.35 mM KCl, 0.5 mM $CaCl_2$, 6 mM $MgCl_2$, 0.6 mM NaH_2PO_4, and 10 mM glucose. Each brain was cut into blocks, and three to four coronal slices (250 μm) were cut with a vibratome (VT1200s, Leica) through the entire rostrocaudal extent of the DRN between −4.84 and −4.48 mm from the bregma. The slices were placed in a submerged chamber for at least 1 hour in artificial cerebrospinal fluid (ACSF) containing 138.6 mM NaCl, 3.35 mM KCl, 2 mM $CaCl_2$, 1.3 mM $MgCl_2$, 21 mM $NaHCO_3$, 0.6 mM $NaH_2PO_4{\cdot}2H_2O$, and 10 mM glucose. The ACSF was maintained at pH 7.4 by bubbling with 95% O_2/5% CO_2 gas.

Individual slices were transferred to a recording chamber attached to a microscope stage and continuously perfused with oxygenated ACSF at a flow rate of 1.4 ml/min and a temperature of 28°C. Borosilicate glass-patch electrodes (World Precision Instruments) were used for whole-cell recordings from DRN cells and had a resistance of 4 to 6 megohms when filled with an internal solution of 150 mM K-methanesulfonate, 1 mM KCl, 0.2 mM K-EGTA, 20 mM Hepes, 3 mM Mg-ATP_2, 0.4 mM Na-GTP, and 15 mM biocytin (pH 7.38). DRN serotonergic cells were visually identified on infrared–differential interference contrast images using a water-immersion objective (40×, numerical aperture of 0.80; Olympus). The recorded neurons were infused with biocytin via the recording patch electrode. After the experiments, immunohistochemical procedures were used to visualize the cell morphology and identify Tph immunoreactivity, which is a marker of 5-HT neurons. Briefly, the slices were immersion-fixed overnight in 4% PFA prepared in 0.1 M PBS and then stored in PBS until use. The fixed sections were incubated with anti-Tph polyclonal antibody for 3 days at 4°C. Subsequently, the sections were incubated with Alexa Fluor 488–conjugated secondary antibody and Alexa Fluor 594–conjugated streptavidin (1:1000 dilution; Life Technologies) to visualize Tph immunohistochemical labeling and biocytin, respectively.

In vitro electrophysiology for L2/3 pyramidal neurons in somatosensory cortex

Male and female P15 to P23 littermate mice were used. Mice were anesthetized with CO_2 gas for decapitation. Cortical slices (300 μm) were prepared as previously described (*43*). The brains were sectioned with VT1000 or VT1200S slicers (Leica Microsystems) in an ice-cold cutting solution containing 120 mM choline-Cl, 2 mM KCl, 8 mM $MgCl_2$, 28 mM $NaHCO_3$, 1.25 mM NaH_2PO_4, and 20 mM glucose bubbled with 95% O_2 and 5% CO_2. For recovery, slices were incubated for 1 hour in a normal external solution containing 125 mM NaCl, 2.5 mM KCl, 2 mM $CaCl_2$, 1 mM $MgSO_4$, 1.25 mM NaH_2PO_4, 26 mM $NaHCO_3$, and 20 mM glucose, which was bubbled continuously with a mixture of 95% O_2 and 5% CO_2 at room temperature.

Whole-cell recordings were made from the somata of L2/3 pyramidal neurons in the S1BF using an upright microscope (BX50WI, Olympus). Pyramidal neurons were identified on the basis of the triangular appearance of the cell soma and the presence of a single apical dendrite as well as electrophysiological properties. All experiments were carried out at 32° ± 1°C. The composition of intracellular solutions were as follows: 35 mM K-D-gluconate, 100 mM KCl, 10 mM NaCl, 10 mM Hepes, 0.5 mM EGTA, 0.34 mM Na_2-GTP, and 4 mM Mg-ATP (pH 7.3 with KOH) for IPSC recording and 140 mM K-D-gluconate, 8 mM KCl, 2 mM NaCl, 0.2 mM EGTA, 10 mM Hepes, 3 mM Mg-ATP, and 0.5 mM Na_2-GTP (pH 7.3 with KOH) for EPSC recording. The membrane potential was held at −80 mV for both EPSC and IPSC recordings. By using the intracellular solution containing high chloride ion, IPSCs were detected as inward currents at a holding potential of −80 mV. Miniature PSCs were recorded in the presence of 0.5 μM tetrodotoxin (TTX) 10 min after the establishment of whole-cell patch clamp. The normal external solution was supplemented with 5 μM (*R*)-3-(2-carboxypiperazin-4-yl)-propyl-1-phosphonic acid and 10 μM 2,3-dioxo-6-nitro-1,2,3,4-tetrahydrobenzo[*f*]quinoxaline-7-sulfonamide for IPSC recording to block NMDA (*N*-methyl-D-aspartate) and AMPA receptors or 50 μM picrotoxin for EPSC recording to block $GABA_A$ receptors. sIPSCs were recorded in the absence of TTX. Ionic currents were recorded with an Axopatch 1D patch-clamp amplifier (Molecular Devices) or EPC10 USB (HEKA). Signals were digitized at 20 kHz for recording-evoked responses or at 40 kHz for recording miniature responses. Online data acquisition and offline data analysis were performed using the PULSE or PATCHMASTER software (HEKA). For electrical stimulation, a stimulating electrode filled with standard saline was placed in L2/3 around recording cells. Electrical stimuli (duration, 0.1 ms; amplitude, 0.8 to 5.5 mA) were applied at 10- to 3000-ms intervals. For acute 5-HT treatment, 10 μM serotonin creatinine sulfate was added in the external bath solution. The sIPSC and mIPSC recordings before 5-HT treatment and 2 to 4 min after treatment were analyzed as pretreatment and 5-HT conditions, respectively. The mIPSCs in saccharin- or FLX-treated mice were recorded in the presence of 0.5 μM TTX, 10 μM 6-cyano-7-nitroquinoxaline-2,3-dione disodium salt hydrate, and 50 μM D-(−)-2-amino-5-phosphonopentanoic acid. Miniature responses were analyzed using Mini Analysis Program (version 6.0.7; Synaptosoft Inc.).

For I_h current analysis, 2 mM 4-aminopyridine, 0.5 mM $BaCl_2$, and 1 μM TTX were added in the external bath solution. The neurons were held at −40 mV and hyperpolarized with 2-s voltage steps from −50 to −120 mV in 10-mV increments. Whole-cell capacitive transients and leak currents were not compensated for in this recording. The I_h currents were calculated by dividing the instantaneous current measured at the beginning of the step by the steady-state current measured at the end of the step. All analyses were performed blind to genotype.

Quantitative analyses of 5-HT and 5-HIAA

The concentrations of 5-HT and 5-HIAA in the midbrain were measured using a high-performance liquid chromatography (HPLC) system (Eicom) as previously described (*36*). The midbrain samples were dissected from 9- to 10-week-old mice and stored at −80°C until use. For analyses, the samples were homogenized in 0.2 M ice-cold perchloric acid, and the homogenates were cooled on ice for 30 min for deproteinization. The homogenates were centrifuged at 20,000*g* for 15 min at 0°C. The pH of the supernatants was adjusted to approximately 3 by adding 1 M sodium acetate, and the pellets were used for protein quantification. The supernatants were filtered through a 0.45-μm filter (Millipore), and 10 μl of the filtrate was applied to the HPLC system. The system had a 3 × 150 mm octadecylsilane column (SC-5ODS, Eicom) and an electrochemical detector (HTEC-500, Eicom) set to an applied potential of 750 mV versus an Ag/AgCl reference analytical electrode. The changes in electric current (in nanoamperes) were recorded using a computer interface. The mobile phase was composed of 0.1 M aceto–citric acid buffer (pH 3.5), methanol, 0.46 M sodium-1-octane sulfonate, and 0.015 mM disodium-EDTA at a ratio of 830:170:1.9:1. The flow rate was 0.5 ml/min. Protein quantification

was performed using a Bio-Rad protein assay system (Bio-Rad) according to the manufacturer's protocol.

Behavioral tests

All behavioral tests were performed between 8:30 a.m. and 2:00 p.m. The procedures were principally based on those described in our previous report (*6*). The observer was blinded to the mouse genotypes until all behavioral tests were finished. All apparatuses and analysis software were products of O'Hara & Co. Ltd.

Open-field test

The open-field test was performed before the 3-CSI test. The plastic open-field chamber was 50 cm (length) × 50 cm (width) × 50 cm (height). The field was illuminated at 40 lux. Behavior was monitored for 15 min and recorded with a charge-coupled device (CCD) camera connected to a personal computer. The total ambulation distance and percentage of time spent in the center of the field were recorded automatically using Image OF software. The center of the field was defined as a central square of 30 cm × 30 cm. The distance traveled in the center area was measured using ImageJ software at offline analysis.

3-CSI test

The apparatus used was a plastic box [40 cm (length) × 60 cm (width) × 20 cm (height)] with two partitions that separated the box into three chambers of the same size. The box was illuminated at 100 lux, and the partitions had openings that allowed the mouse to move freely from one chamber to another. Wire cages [11 cm (height) × 9 cm (diameter)] were placed at the left corner of the left chamber and at the right corner of the right chamber. Before the test, each subject mouse was allowed to acclimate to the test box by free exploration for 5 min. Subsequently, an unfamiliar younger WT C57BL/6J male mouse (stranger mouse) that had no previous contact with the subject mouse was placed in the wire cage at one corner, whereas the cage at the opposite corner remained empty. The locations of the stranger mouse and the empty cage were alternated between the left and right chambers on consecutive sessions. At the beginning of the test, the subject mouse was placed in the middle chamber and allowed to move freely throughout all three chambers. During a 10-min session, the behavior was recorded, and the time spent in the interaction zone (approaching time), which is defined as an area within 9 cm from the edge of the wire cage, was measured automatically using Image CSI software.

MWM test

The visible platform, hidden platform, probe test, and reversal probe test components of the MWM test were conducted. A circular pool [100 cm (diameter) × 20 cm (height)] filled with water (23° ± 0.5°C) was used for the tests. Each training trial began by placing the mouse into the quadrant that was adjacent right, adjacent left, or opposite to the target quadrant containing the platform (10 cm in diameter and 1 cm beneath the water surface), in a semi-random order. A different order of the start positions was applied every day, but the identical order of start positions was used for all mice. The training trials were 60 s in maximum duration. A mouse that failed to reach the platform within 60 s was subsequently guided to the platform. Four trials per day (25-min intervals between trials) were conducted for six successive days for acquisition of the hidden platform test with the original platform location and four successive days with a new platform location (reversal probe test) rotated 180° from the original platform location. At 1 hour after the end of the 6th day and 10th day of hidden platform training, a probe test and a reversal probe test were conducted for 1 min to confirm that these spatial learning tests were acquired on the basis of navigation by distal environmental room cues, respectively. The time spent in each quadrant and numbers of crossings above the former target site were automatically recorded with a CCD camera connected to a personal computer and analyzed by TimeWMZ software. We excluded data from mice that stopped searching for the platform and floated in the water for more than 5 s in the probe tests.

USV test

Both male and female pups (P7) were used. To examine the effect of FLX dosage, we treated the pups daily (from P1 to P6) with FLX (0.5 or 2.5 mg/kg dose diluted in PBS) by intraperitoneal injection. On the day of the study, the pups with their mother were moved to the experimental room at least 60 min before the initiation of the study. After habituation, each pup was removed from its mother and placed in a stainless steel cylinder [7.5 cm (diameter) × 7 cm (height)] on the COOL PLATE (NCP-2215, Nisshin Rika Co. Ltd.), which maintained a cylinder temperature of 25°C in a soundproof room (AT-81, RION Co. Ltd.). The number of vocalization was measured for 5 min. Individual calls made by each pup were collected by an ultrasound-detectable microphone (UC-29, RION Co. Ltd.) and then amplified by a preamplifier (NH-05A, RION Co. Ltd.) and a main amplifier (UN-04A, RION Co. Ltd.) with a high-pass filter (1.5 kHz; Multifunction filter 3611, NF Co. Ltd.). Then, analog signals were converted to digital signals by an analog-to-digital converter (CH-3150, Exacq Technologies Inc.) and stored in a personal computer. The numbers of vocalizations were counted by the recording software (Dasy Lab 9.0, measX GmbH and Co. KG) with a digital filter at 20 kHz to count the vocalizations generated at the ultrasound range. In the case of power spectrum analysis, stored signals were transformed with the fast Fourier transform method by the MATLAB software and visualized by SASLab Pro (Avisoft Bioacoustics).

Statistics

Data sets were first tested for normality using a Shapiro-Wilk normality test, and then equal variances were tested using an *F* test in the case of two-group comparison or a Bartlett test in the case of multiple comparison. If the data sets fit a normal distribution, a parametric method was used, and if not, a nonparametric method was used. A two-tailed Student's *t* test and Wilcoxon rank sum test for the data sets with equal variances and a two-tailed Welch's *t* test and Brunner-Munzel test for the data sets with non-equal variances were used in parametric and nonparametric analyses, respectively. For multiple comparison tests, a Steel test or a Steel-Dwass test was used for the data sets with non-normality and equal variances, and a Games-Howell test was used when the criteria of normality and equal variance were not satisfied. A two-tailed paired *t* test and exact Wilcoxon signed-rank test were used for comparison of paired samples. A two-sample Kolmogorov-Smirnov test was used for morphological analysis of 5-HT neurons. For the analysis of gene expression, *P* value was corrected with the Holm method. Two-way repeated-measures ANOVA was used for comparison of dendritic blanch interactions and I_h currents of pyramidal neurons. In PET imaging, a statistically significant difference in the rCGM between WT and *15q dup* mice was defined at a threshold of $P < 0.005$ (uncorrected). The analyses described above were performed with GraphPad software, StatView software, or R version 3.3.2 (The R Foundation for Statistical Computing). Differences were considered to be statistically nonsignificant when $P > 0.05$. All statistical results are described in table S3.

SUPPLEMENTARY MATERIALS

Supplementary material for this article is available at http://advances.sciencemag.org/cgi/content/full/3/6/e1603001/DC1

fig. S1. Dendritic morphology of lwDRN 5-HT neurons shows no difference between WT and *15q dup* mice.
fig. S2. Cell densities of inhibitory neurons are unchanged in *15q dup* mice.
fig. S3. The number of symmetry synapses is decreased in the S1BF of *15q dup* mice.
fig. S4. The paired-pulse ratio of inhibitory transmissions in S1BF L2/3 pyramidal neurons is not changed in *15q dup* mice.
fig. S5. *15q dup* S1BF have differential expression of $GABA_A$ receptor subunits.
fig. S6. *15q dup* mice have decreased dendritic length of S1BF L2/3 pyramidal neurons.
fig. S7. Profiling of 5-HT receptor expression in *15q dup* brain.
fig. S8. Acute 5-HT application enhances inhibitory transmission and suppresses excitability of S1BF L2/3 pyramidal neurons in *15q dup* mice.
table S1. Properties of action potentials of 5-HT neurons in DRN.
table S2. Firing properties of L2/3 regular spiking neurons in vivo.
table S3. Statistical results.
Supplementary Methods
References (*44*, *45*)

REFERENCES AND NOTES

1. D. Malhotra, J. Sebat, CNVs: Harbingers of a rare variant revolution in psychiatric genetics. *Cell* **148**, 1223–1241 (2012).
2. T. Bourgeron, From the genetic architecture to synaptic plasticity in autism spectrum disorder. *Nat. Rev. Neurosci.* **16**, 551–563 (2015).
3. L. de la Torre-Ubieta, H. Won, J. L. Stein, D. H. Geschwind, Advancing the understanding of autism disease mechanisms through genetics. *Nat. Med.* **22**, 345–361 (2016).
4. J. A. S. Vorstman, W. G. Staal, E. van Daalen, H. van Engeland, P. F. R. Hochstenbach, L. Franke, Identification of novel autism candidate regions through analysis of reported cytogenetic abnormalities associated with autism. *Mol. Psychiatry* **11**, 18–28 (2006).
5. V. M. Leppa, S. N. Kravitz, C. L. Martin, J. Andrieux, C. Le Caignec, D. Martin-Coignard, C. DyBuncio, S. J. Sanders, J. K. Lowe, R. M. Cantor, D. H. Geschwind, Rare inherited and de novo CNVs reveal complex contributions to ASD risk in multiplex families. *Am. J. Hum. Genet.* **99**, 540–554 (2016).
6. J. Nakatani, K. Tamada, F. Hatanaka, S. Ise, H. Ohta, K. Inoue, S. Tomonaga, Y. Watanabe, Y. J. Chung, R. Banerjee, K. Iwamoto, T. Kato, M. Okazawa, K. Yamauchi, K. Tanda, K. Takao, T. Miyakawa, A. Bradley, T. Takumi, Abnormal behavior in a chromosome-engineered mouse model for human 15q11-13 duplication seen in autism. *Cell* **137**, 1235–1246 (2009).
7. K. Tamada, S. Tomonaga, F. Hatanaka, N. Nakai, K. Takao, T. Miyakawa, J. Nakatani, T. Takumi, Decreased exploratory activity in a mouse model of 15q duplication syndrome; implications for disturbance of serotonin signaling. *PLOS ONE* **5**, e15126 (2010).
8. M. Isshiki, S. Tanaka, T. Kuriu, K. Tabuchi, T. Takumi, S. Okabe, Enhanced synapse remodelling as a common phenotype in mouse models of autism. *Nat. Commun.* **5**, 4742 (2014).
9. C. Piochon, A. D. Kloth, G. Grasselli, H. K. Titley, H. Nakayama, K. Hashimoto, V. Wan, D. H. Simmons, T. Eissa, J. Nakatani, A. Cherskov, T. Miyazaki, M. Watanabe, T. Takumi, M. Kano, S. S.-H. Wang, C. Hansel, Cerebellar plasticity and motor learning deficits in a copy-number variation mouse model of autism. *Nat. Commun.* **5**, 5586 (2014).
10. J. Ellegood, N. Nakai, J. Nakatani, M. Henkelman, T. Takumi, J. Lerch, Neuroanatomical phenotypes are consistent with autism-like behavioral phenotypes in the 15q11-13 duplication mouse model. *Autism Res.* **8**, 545–555 (2015).
11. D. C. Chugani, Neurotransmitters, in *Autism Spectrum Disorders,* D. G. Amaral, G. Dawson, D. H. Geschwind, Eds. (Oxford Univ. Press, 2011), pp. 566–575.
12. E. M. Daly, Q. Deeley, C. Ecker, M. Craig, B. Hallahan, C. Murphy, P. Johnston, D. Spain, N. Gillan, M. Brammer, V. Giampietro, M. Lamar, L. Page, F. Toal, A. Cleare, S. Surguladze, D. G. M. Murphy, Serotonin and the neural processing of facial emotions in adults with autism: An fMRI study using acute tryptophan depletion. *Arch. Gen. Psychiatry* **69**, 1003–1013 (2012).
13. K.-P. Lesch, J. Waider, Serotonin in the modulation of neural plasticity and networks: Implications for neurodevelopmental disorders. *Neuron* **76**, 175–191 (2012).
14. P. J. Uhlhaas, W. Singer, Neuronal dynamics and neuropsychiatric disorders: Toward a translational paradigm for dysfunctional large-scale networks. *Neuron* **75**, 963–980 (2012).
15. S. Han, C. Tai, R. E. Westenbroek, F. H. Yu, C. S. Cheah, G. B. Potter, J. L. Rubenstein, T. Scheuer, H. O. de la Iglesia, W. A. Catterall, Autistic-like behaviour in *Scn1a*$^{+/-}$ mice and rescue by enhanced GABA-mediated neurotransmission. *Nature* **489**, 385–390 (2012).
16. R. Tyzio, R. Nardou, D. C. Ferrari, T. Tsintsadze, A. Shahrokhi, S. Eftekhari, I. Khalilov, V. Tsintsadze, C. Brouchoud, G. Chazal, E. Lemonnier, N. Lozovaya, N. Burnashev, Y. Ben-Ari, Oxytocin-mediated GABA inhibition during delivery attenuates autism pathogenesis in rodent offspring. *Science* **343**, 675–679 (2014).
17. N. Gogolla, A. E. Takesian, G. Feng, M. Fagiolini, T. K. Hensch, Sensory integration in mouse insular cortex reflects GABA circuit maturation. *Neuron* **83**, 894–905 (2014).
18. E. S. B. van Kleef, P. Gaspar, A. Bonnin, Insights into the complex influence of 5-HT signaling on thalamocortical axonal system development. *Eur. J. Neurosci.* **35**, 1563–1572 (2012).
19. I. Dinstein, D. J. Heeger, L. Lorenzi, N. J. Minshew, R. Malach, M. Behrmann, Unreliable evoked responses in autism. *Neuron* **75**, 981–991 (2012).
20. C. McCormick, D. Hessl, S. L. Macari, S. Ozonoff, C. Green, S. J. Rogers, Electrodermal and behavioral responses of children with autism spectrum disorders to sensory and repetitive stimuli. *Autism Res.* **7**, 468–480 (2014).
21. L. Tremere, T. P. Hicks, D. D. Rasmusson, Role of inhibition in cortical reorganization of the adult raccoon revealed by microiontophoretic blockade of $GABA_A$ receptors. *J. Neurophysiol.* **86**, 94–103 (2001).
22. E. Foeller, T. Celikel, D. E. Feldman, Inhibitory sharpening of receptive fields contributes to whisker map plasticity in rat somatosensory cortex. *J. Neurophysiol.* **94**, 4387–4400 (2005).
23. D. D. Dunning, C. L. Hoover, I. Soltesz, M. A. Smith, D. K. O'Dowd, $GABA_A$ receptor–mediated miniature postsynaptic currents and α-subunit expression in developing cortical neurons. *J. Neurophysiol.* **82**, 3286–3297 (1999).
24. F. Yi, T. Danko, S. C. Botelho, C. Patzke, C. Pak, M. Wernig, T. C. Südhof, Autism-associated SHANK3 haploinsufficiency causes I_h channelopathy in human neurons. *Science* **352**, aaf2669 (2016).
25. P. Zhong, Z. Yan, Differential regulation of the excitability of prefrontal cortical fast-spiking interneurons and pyramidal neurons by serotonin and fluoxetine. *PLOS ONE* **6**, e16970 (2011).
26. L. M. Hurley, D. M. Devilbiss, B. D. Waterhouse, A matter of focus: Monoaminergic modulation of stimulus coding in mammalian sensory networks. *Curr. Opin. Neurobiol.* **14**, 488–495 (2004).
27. J. L. R. Rubenstein, M. M. Merzenich, Model of autism: Increased ratio of excitation/inhibition in key neural systems. *Genes Brain Behav.* **2**, 255–267 (2003).
28. Z. Zhang, Q.-Q. Sun, The balance between excitation and inhibition and functional sensory processing in the somatosensory cortex. *Int. Rev. Neurobiol.* **97**, 305–333 (2011).
29. J. S. Isaacson, M. Scanziani, How inhibition shapes cortical activity. *Neuron* **72**, 231–243 (2011).
30. M. V. Puig, A. Watakabe, M. Ushimaru, T. Yamamori, Y. Kawaguchi, Serotonin modulates fast-spiking interneuron and synchronous activity in the rat prefrontal cortex through 5-HT_{1A} and 5-HT_{2A} receptors. *J. Neurosci.* **30**, 2211–2222 (2010).
31. O. Yizhar, L. E. Fenno, M. Prigge, F. Schneider, T. J. Davidson, D. J. O'Shea, V. S. Sohal, I. Goshen, J. Finkelstein, J. T. Paz, K. Stehfest, R. Fudim, C. Ramakrishnan, J. R. Huguenard, P. Hegemann, K. Deisseroth, Neocortical excitation/inhibition balance in information processing and social dysfunction. *Nature* **477**, 171–178 (2011).
32. M. L. McPheeters, Z. Warren, N. Sathe, J. L. Bruzek, S. Krishnaswami, R. N. Jerome, J. Veenstra-VanderWeele, A systematic review of medical treatments for children with autism spectrum disorders. *Pediatrics* **127**, e1312–e1321 (2011).
33. R. E. Mercer, E. M. Kwolek, J. M. Bischof, M. van Eede, R. M. Henkelman, R. Wevrick, Regionally reduced brain volume, altered serotonin neurochemistry, and abnormal behavior in mice null for the circadian rhythm output gene *Magel2*. *Am. J. Med. Genet. B Neuropsychiatr. Genet.* **150B**, 1085–1099 (2009).
34. S. Zanella, F. Watrin, S. Mebarek, F. Marly, M. Roussel, C. Gire, G. Diene, M. Tauber, F. Muscatelli, G. Hilaire, Necdin plays a role in the serotonergic modulation of the mouse respiratory network: Implication for Prader-Willi syndrome. *J. Neurosci.* **28**, 1745–1755 (2008).
35. E. Al Ageeli, S. Drunat, C. Delanoë, L. Perrin, C. Baumann, Y. Capri, J. Fabre-Teste, A. Aboura, C. Dupont, S. Auvin, L. El Khattabi, D. Chantereau, A. Moncla, A.-C. Tabet, A. Verloes, Duplication of the 15q11-q13 region: Clinical and genetic study of 30 new cases. *Eur. J. Med. Genet.* **57**, 5–14 (2014).
36. M. Nagano, M. Liu, H. Inagaki, T. Kawada, H. Suzuki, Early intervention with fluoxetine reverses abnormalities in the serotonergic system and behavior of rats exposed prenatally to dexamethasone. *Neuropharmacology* **63**, 292–300 (2012).
37. H. Mizuma, M. Shukuri, T. Hayashi, Y. Watanabe, H. Onoe, Establishment of in vivo brain imaging method in conscious mice. *J. Nucl. Med.* **51**, 1068–1075 (2010).
38. H. Monai, M. Ohkura, M. Tanaka, Y. Oe, A. Konno, H. Hirai, K. Mikoshiba, S. Itohara, J. Nakai, Y. Iwai, H. Hirase, Calcium imaging reveals glial involvement in transcranial direct current stimulation-induced plasticity in mouse brain. *Nat. Commun.* **7**, 11100 (2016).
39. Y. Kawamura, H. Nakayama, K. Hashimoto, K. Sakimura, K. Kitamura, M. Kano, Spike timing-dependent selective strengthening of single climbing fibre inputs to Purkinje cells during cerebellar development. *Nat. Commun.* **4**, 2732 (2013).
40. T. W. Margrie, M. Brecht, B. Sakmann, In vivo, low-resistance, whole-cell recordings from neurons in the anaesthetized and awake mammalian brain. *Pflugers Arch.* **444**, 491–498 (2002).

41. D. J. Simons, Multi-whisker stimulation and its effects on vibrissa units in rat SmI barrel cortex. *Brain Res.* **276**, 178–182 (1983).
42. Y. Gocho, A. Sakai, Y. Yanagawa, H. Suzuki, F. Saitow, Electrophysiological and pharmacological properties of GABAergic cells in the dorsal raphe nucleus. *J. Physiol. Sci.* **63**, 147–154 (2013).
43. A. Agmon, B. W. Connors, Thalamocortical responses of mouse somatosensory (barrel) cortex in vitro. *Neuroscience* **41**, 365–379 (1991).
44. D. T. Wong, F. P. Bymaster, J. S. Horng, B. B. Molloy, A new selective inhibitor for uptake of serotonin into synaptosomes of rat brain: 3-(p-trifluoromethylphenoxy). N-methyl-3-phenylpropylamine. *J. Pharmacol. Exp. Ther.* **193**, 804–811 (1975).
45. J.-C. Alvarez, D. Bothua, I. Collignon, C. Advenier, O. Spreux-Varoquaux, Determination of fluoxetine and its metabolite norfluoxetine in serum and brain areas using high-performance liquid chromatography with ultraviolet detection. *J. Chromatogr. B Biomed. Sci. Appl.* **707**, 175–180 (1998).

Acknowledgments: We thank C. Yokoyama and H. Monyer for helpful comments and editing of the manuscript and the entire technical staff of the Takumi Lab for technical assistance. **Funding:** This work was supported in part by KAKENHI (Grants-in-Aid for Scientific Research) (grants 25117006, 25460345, 26250014, 26461554, 16H06316, 16H06463, 16K13110, and 16K19066) from the Japan Society of Promotion of Science and the Ministry of Education, Culture, Sports, Science, and Technology; the Strategic International Cooperative Program and Core Research for Evolutional Science and Technology from the Japan Science and Technology Agency; an Intramural Research Grant for Neurological and Psychiatric Disorders of the National Center of Neurology and Psychiatry; the Takeda Science Foundation; and Takeda Pharmaceutical Co. Ltd. **Author contributions:** N.N., F.S., Y.K., H. Monai, H.H., K.K., M.K., K.H., and H.S. designed, performed, and analyzed electrophysiological and calcium imaging experiments. M.N., A.K., K.T., H.I., T.K., and H.S. designed, performed, and analyzed behavioral and neurochemical experiments. N.N., Yasuhito Watanabe, T.M., M.W., Y.S., and S.O. designed, performed, and analyzed histological experiments. H. Mizuma, H.O., and Yasuyoshi Watanabe designed, performed, and analyzed PET experiments. N.N., Yasuhito Watanabe, and J.N. designed, performed, and analyzed molecular biological experiments. T.T. supervised the research. N.N., M.N., F.S., Yasuhito Watanabe, H.S., and T.T. wrote the manuscript with input from all authors. All authors discussed and commented on the results and the manuscript. **Competing interests:** The authors declare that they have no competing interests. **Data and materials availability:** All data needed to evaluate the conclusions in the paper are present in the paper and/or the Supplementary Materials. Additional data related to this paper may be requested from the authors.

Submitted 30 November 2016
Accepted 26 April 2017
Published 21 June 2017
10.1126/sciadv.1603001

Citation: N. Nakai, M. Nagano, F. Saitow, Y. Watanabe, Y. Kawamura, A. Kawamoto, K. Tamada, H. Mizuma, H. Onoe, Y. Watanabe, H. Monai, H. Hirase, J. Nakatani, H. Inagaki, T. Kawada, T. Miyazaki, M. Watanabe, Y. Sato, S. Okabe, K. Kitamura, M. Kano, K. Hashimoto, H. Suzuki, T. Takumi, Serotonin rebalances cortical tuning and behavior linked to autism symptoms in 15q11-13 CNV mice. *Sci. Adv.* **3**, e1603001 (2017).